



**HAL**  
open science

## Impact of agricultural atmospheric pollutants on the opto-electrical performance of CIGS solar cells

Adèle Debono, Noor Fikree, Arthur Julien, Amelle Rebai, Nao Harada,  
Nathanaelle Schneider, Jean-françois Guillemoles, Polina Volovitch

### ► To cite this version:

Adèle Debono, Noor Fikree, Arthur Julien, Amelle Rebai, Nao Harada, et al.. Impact of agricultural atmospheric pollutants on the opto-electrical performance of CIGS solar cells. *Progress in Photo-voltaics*, 2024, 32 (11), pp.814-826. 10.1002/pip.3834 . hal-04779991

**HAL Id: hal-04779991**

**<https://hal.science/hal-04779991v1>**

Submitted on 14 Nov 2024

**HAL** is a multi-disciplinary open access archive for the deposit and dissemination of scientific research documents, whether they are published or not. The documents may come from teaching and research institutions in France or abroad, or from public or private research centers.

L'archive ouverte pluridisciplinaire **HAL**, est destinée au dépôt et à la diffusion de documents scientifiques de niveau recherche, publiés ou non, émanant des établissements d'enseignement et de recherche français ou étrangers, des laboratoires publics ou privés.



Distributed under a Creative Commons Attribution 4.0 International License

# Impact of agricultural atmospheric pollutants on the optoelectrical performance of CIGS solar cells

Adèle Debono<sup>1,2</sup>  | Noor Fikree<sup>1,2</sup> | Arthur Julien<sup>2,3</sup>  | Amelle Rebai<sup>2</sup> |  
 Nao Harada<sup>3</sup> | Nathanaelle Schneider<sup>2</sup> | Jean-François Guillemoles<sup>2</sup> |  
 Polina Volovitch<sup>1</sup> 

<sup>1</sup>Chimie ParisTech-CNRS, PSL Research University, Institut de Recherche de Chimie Paris (IRCP), Paris, France

<sup>2</sup>Institut Photovoltaïque d'Île-de-France (IPVF), UMR 9006, CNRS, Ecole Polytechnique - IP Paris, Chimie Paristech - PSL, Palaiseau, France

<sup>3</sup>IPVF, Institut Photovoltaïque d'Île-de-France, Palaiseau, France

## Correspondence

Adèle Debono and Jean-François Guillemoles, Institut Photovoltaïque d'Île-de-France (IPVF), UMR 9006, CNRS, Ecole Polytechnique - IP Paris, Chimie Paristech - PSL, Palaiseau, 91120, France.

Email: [adele.debono@chimieparistech.psl.eu](mailto:adele.debono@chimieparistech.psl.eu) and [jean-francois.guillemoles@cnrs.fr](mailto:jean-francois.guillemoles@cnrs.fr)

Polina Volovitch, Chimie ParisTech-CNRS, PSL Research University, Institut de Recherche de Chimie Paris (IRCP), 11 rue Pierre et Marie Curie, 75005 Paris, France.

Email: [polina.volovitch@chimieparistech.psl.eu](mailto:polina.volovitch@chimieparistech.psl.eu)

## Abstract

The reliability of CIGS solar systems in agricultural environments was investigated using an accelerated aging test. Both complete cells and representative stacks of selected layers and interfaces were exposed to humidity and temperature variations for 9 to 14 days with and without ammonium sulfate ( $(\text{NH}_4)_2\text{SO}_4$ ), an aerosol pollutant representative of agricultural activities. The performance evolution of complete cells was evaluated by J-V curves and EQE measurements. After 9 days, the presence of  $(\text{NH}_4)_2\text{SO}_4$  led to a performance loss of 58%, significantly higher than the 37% loss observed without pollutants. Using computer calculations based on the two-diode model, it was possible to de-correlate some interactions between J-V parameters. The results of modeling suggested that the pollutant caused optical losses and conductivity loss of electrical contacts, presumably by corrosion. Sheet resistance and Hall effect measurements on the representative stacks of layers confirmed that the conductivity loss of ZnO:Al (AZO) after 14 days of aging strongly impacted the cell performance, this phenomenon being even more severe in the presence of  $(\text{NH}_4)_2\text{SO}_4$ . The conductivity of Mo remained significantly less affected by aging both with and without pollutants. The NiAlNi contacts after aging with  $(\text{NH}_4)_2\text{SO}_4$  became so resistive that measurement was impossible. Corroborating modeling and experimental results, the drop in  $J_{\text{sc}}$  was attributed to the loss of the interference fringes in the AZO rather than to the loss of optical transmittance. Finally, aging without pollutants mostly impacted  $V_{\text{oc}}$  and  $R_{\text{sh}}$  due to the formation of shunt paths.

## KEYWORDS

agrivoltaics, atmospheric pollutant, CIGS solar cells, degradation, outdoor durability, performance

## 1 | INTRODUCTION

In photovoltaic (PV) installations, product warranty is a key element for their development, ensuring that modules will operate at over

80% of their initial rated efficiency for 25 to 30 years. However, in the existing reliability approaches the impact of atmospheric pollutants is rarely considered in the PV domain. Research rather focuses on the optical losses induced by the pollutants, such as alteration of

This is an open access article under the terms of the [Creative Commons Attribution](https://creativecommons.org/licenses/by/4.0/) License, which permits use, distribution and reproduction in any medium, provided the original work is properly cited.

© 2024 The Author(s). Progress in Photovoltaics: Research and Applications published by John Wiley & Sons Ltd.

the radiation spectrum [1,2] or dust deposition [3–5]. A few pioneering works have considered the effect of atmospheric gases on the chemical and electrical stability of solar cells [6]. Our group [7,8] recently demonstrated the importance of atmospheric aerosols for the stability of solar cell materials and some representative interfaces. With the development of PV applications in agricultural areas (agrivoltaics), the impact of atmospheric pollutants issued from agricultural activity on the stability of solar cells becomes essential. However, to the best of our knowledge, the effect of atmospheric aerosol pollutants on the entire solar cell performance has never been studied.

Cu (In,Ga)Se<sub>2</sub> (CIGS) thin films represent an efficient and attractive technology for lightweight and flexible designs, well suited for agrivoltaic applications, and already available on the market [9]. In agricultural environments, one of the most known pollutants is ammonium sulfate (NH<sub>4</sub>)<sub>2</sub>SO<sub>4</sub>, a volatile aerosol released by agricultural activities or formed in the atmosphere from agricultural gas emissions. (NH<sub>4</sub>)<sub>2</sub>SO<sub>4</sub> can be directly used as a fertilizer for alkaline soils [10] and as a spray adjuvant [11]. It can also be formed from the ammonia gas (NH<sub>3</sub>), emitted by animal manure and urea, reacting with sulfuric acid H<sub>2</sub>SO<sub>4</sub> [12,13]. When the aerosol is deposited on the ground by dry deposition or wet deposition through rainwater (between 17 and 170 μg·cm<sup>-2</sup> of NH<sub>4</sub><sup>+</sup> and 57 to 500 μg·cm<sup>-2</sup> of SO<sub>4</sub><sup>2-</sup> per year [14–17]), it causes the acidification of the surface water [17] but also atmospheric corrosion of diverse materials [18].

In this work, we investigated the effects of (NH<sub>4</sub>)<sub>2</sub>SO<sub>4</sub> pollution on the stability of chalcopyrite Cu (In<sub>x</sub>Ga<sub>[1-x]</sub>)Se<sub>2</sub> (CIGS)-based thin film photovoltaic cell under different conditions of temperature and humidity. In our previous works [7,8], we demonstrated that 25 nm thick Al<sub>2</sub>O<sub>3</sub> encapsulation was sensitive to (NH<sub>4</sub>)<sub>2</sub>SO<sub>4</sub> aerosols. From both fundamental and industrial points of view, it becomes important to understand how unencapsulated cells would behave if the encapsulation failed. For these purposes, additional elements in reliability tests could challenge the established standards.

The mechanistic interpretation of the results of the accelerated tests is also challenging. In the literature, the degradation of CIGS solar cells is primarily observed through optoelectrical J-V parameters allowing to correlate the observed change with physical processes occurring inside the cell. Various numerical models are usually employed to link material properties to optoelectrical performances. In particular, drift-diffusion simulations, which completely resolve the charge carrier behavior, give access to numerous material properties in the cell. Such an approach can be employed by comparing simulations of fresh and degraded samples with the results of the experimental ex situ characterizations [19], or to investigate degradation trends in parametric studies [20,21]. The complexity of these models requires, however, elaborated fitting procedures and careful design of the inputs. Notably, statistical approaches can be employed to minimize associated uncertainties, subsequently allowing to simulate and compare degradation mechanisms with experimental results [22]. Simpler approaches such as a diode model have also been employed [23]. Their simplicity allows us to couple them with the models describing supplementary phenomena, such as thermal models to understand the formation of hotspots [24]. Rin and Han coupled a distributed diode

model with modeling of diffusion processes to account for water ingress into the solar cell [25]. Modeling approaches generally suppose a prior knowledge of the mechanisms in play. Finally, specific models for the degradation kinetics [26] or for the diffusion of species inside the solar cell [27] can lead to interesting reproductions of the observed degradation trends. However, they often rely on simplifications of the processes or even strong assumptions on the nature of the degradation processes at stake.

The main objective of this work is to propose a systematic methodology able to take into account the effect of atmospheric pollutants on the performance (power conversion efficiency, short-circuit current  $J_{sc}$ , open-circuit voltage  $V_{oc}$  or fill factor FF ...) of thin layer CIGS solar cells. It is subdivided into several goals:

1. Determine whether the presence of ammonium sulfate, largely used as nitrogen and sulfur fertilizer and generated in agricultural environments, can impact the performance of CIGS solar cells.
2. Propose a computer model based on electrical data to formulate hypotheses of opto-electric deterioration pathways and propose the most critical for degradation layers or interfaces.
3. Check the validity of the computer model by comparing the results with the experimentally observed opto-electric degradation via the use of specific samples representative stacks of materials and interfaces.

## 2 | MATERIALS AND METHODS

### 2.1 | Sample architecture and fabrication

The investigated samples were composed of complete CIGS minimodules SLG/Mo/CIGS/Zn(O,S)/ZnMgO/AZO/NiAlNi (composed of 10 cells) and representative stacks of only a few layers as presented in Figure 1. All samples were prepared on 3 mm soda lime glass (SLG). 600-nm molybdenum (Mo) thin films were deposited by direct current magnetron sputtering, 2-μm CIGS by co-evaporation, 50-nm zinc oxide (i:ZnO), 480-nm aluminum-doped zinc oxide (AZO) by atomic layer deposition and front contact 50/600/50-nm nickel/aluminum/nickel (NiAlNi) by evaporation. For the modules, the 20 nm-Zn(O,S) layer was chemical bath deposited, and the 40 to 70 nm-ZnMgO and the 300 nm-AZO were sputtered. Detailed descriptions of the film preparation procedures can be found in Supporting Information (SI).

### 2.2 | Accelerated degradation protocol

The aging protocol was described in detail elsewhere [7,8] and its schematic representation can be found in SI, Figure S1. Samples were aged in a Weiss WKL 100 climatic chamber until significant degradation of opto-electric characteristics could be detected. This time was different for complete cells and model stacks. For the minimodules only 9 days of aging degraded cell efficiency and the

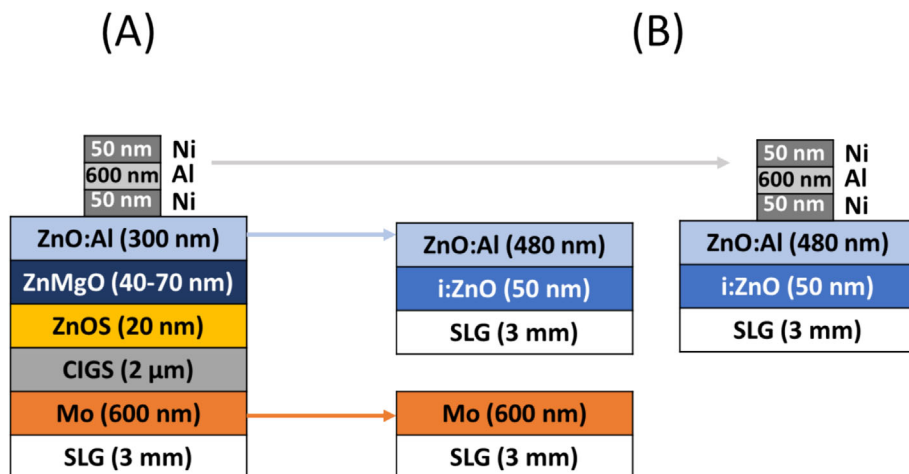


**FIGURE 1** Schematics of the sample configurations of (A) complete cell (SLG/Mo/CIGS/Zn(O,S)/ZnMgO/AZO/NiAlNi) and (B) representative models: SLG/Mo, SLG/i:ZnO/AZO and SLG/i:ZnO/AZO/NiAlNi.

parameters extracted from J-V curves so strongly that the experiment was stopped at 9 days. It was evidently impossible to measure J-V curves for model stacks of individual layers without n-layer. The aging time was chosen for 14 days for representative stacks to push degradation of each configuration and not to limit the mechanistic understanding to the detection of the most fragile layer/interface. Results of both visual observations and opto-electrical measurements suggested that the degradation of isolated stacks was slower than the degradation of the complete minimodules but with similar degradation mechanisms. Twenty-four hour-cycles of temperature and humidity variation (between 25°C, 85% Relative Humidity [RH] and 80°C, 30% RH) were applied to model day/night or seasonal variations. Wet deposition of atmospheric aerosol was simulated by the daily deposition of a 100 microliter drop of an aqueous solution containing 0.78 mmol. L<sup>-1</sup> of (NH<sub>4</sub>)<sub>2</sub>SO<sub>4</sub> for 5 days. This concentration corresponds to 11.2 μg.cm<sup>-2</sup> per drop of NH<sub>4</sub><sup>+</sup> and 15.0 μg.cm<sup>-2</sup> per drop of SO<sub>4</sub><sup>2-</sup> and represents approximately one year of NH<sub>4</sub><sup>+</sup> deposition (on the lower limit side of 17–170 μg.cm<sup>-2</sup>.year<sup>-1</sup> deposition rates reported in the literature [14–17]). The amount of sulfate ions is, however, much less than its annual deposition rate of (60–500 μg.cm<sup>-2</sup>.year<sup>-1</sup>) but it was dictated by the stoichiometry of (NH<sub>4</sub>)<sub>2</sub>SO<sub>4</sub>. This concentration of 5 years of pollutant was chosen to match the assumption that damp heat test during 1,000 h models 20 years in operation [28]. Assuming a linear correlation between time and degradation, 14 days could correspond to 7 years and 9 days to 4.5 year of in-field operation. Such a correlation should however be taken with caution. First, usually, degradation does not increase linearly with time, so the rate law could be more complex. Second, if the degradation mechanism is affected by the pollutant, the degradation rate could evolve differently with time. Finally, the real conditions cannot be modeled only by selected three parameters (T°C, RH, presence of pollution) and the time of the accelerated test should be more regarded as an indication that as a quantitative estimation of the lifetime of the system in operation. “Reference” samples were stored in a vacuum desiccator at room temperature and “Blank” samples were aged under the same conditions as “(NH<sub>4</sub>)<sub>2</sub>SO<sub>4</sub>” but without drop deposition.

### 2.3 | Physical characterization of cells and layers properties

The performance of the cells was evaluated by current–voltage (J-V) curves and External Quantum Efficiency (EQE) measurements. The quality of the layers was evaluated using ultraviolet–visible–near-infrared (UV–vis–NIR) spectrophotometry, and resistivity measurements. J-V curves were measured before (day 0 noted later as d0) and after 9 days (noted later as d9) aging while the other characterizations of the unaged samples were conducted on the “Reference” samples.

J-V measurements were done under Standard Test Conditions (AM 1.5G, 1,000 W.m<sup>-2</sup>, 25°C) using an Oriel Sol 3A™ (Newport) solar simulator (class AAA) with a voltage step of 50 mV and a scan rate of 100 mV/s, after 1 h of light soaking. EQE spectra were measured on an Oriel IQE 200™ (Newport) with a wavelength step of 10 nm, after 1 h of light soaking. The internal quantum efficiency IQE(λ) was calculated as the ratio between EQE(λ) on 1-Reflectance (λ). Contact conductivity was evaluated by measuring the sheet resistance, R<sub>sheet</sub>, using an in-line four-point probe (Lucas Labs Pro 4 test system). For greater precision, measurements were performed at 20 different locations and the results were expressed as the mean values and standard deviations. Additional evaluation of the sheet resistance R<sub>sheet</sub>, carrier concentration n<sub>Hall</sub>, and Hall mobility μ<sub>Hall</sub> were measured by the Hall effect, at room temperature using an Ecopia AMP55T and HMS-3000 equipment. The optical transmittance and reflectance were collected using an Agilent Cary 5,000 UV–Vis–NIR spectrophotometer equipped with an Agilent Diffuse Reflectance accessory. A mask with a 4-mm diameter circular hole was used to define the probing area. The optical band gap was determined by the intercept of the linear region of the Tauc plot (αhv)<sup>n</sup> against hv with n = 2 because ZnO is considered as a direct band gap semiconductor. The refractive index was calculated using the Swanepoel method and the thickness of the thin film was calculated based on Bragg's law [29,30]. A small measurement artefact was visible on the spectra at 800 nm which was due to a change of the detector. The hyperspectral photoluminescent setup consisted of a hyperspectral imager (Grand-EOS from Photon Etc.) equipped

with an InGaAs camera Zephyr 1.7 both from PhotonEtc which allows acquiring large-size images (15x15 cm<sup>2</sup>) with a resolution of 300 μm per pixel. Spectral acquisitions were done in the range of 900–1,600 nm with a spectral resolution of 2 nm. The samples were uniformly illuminated with light-emitting diodes (LEDs) at a wavelength of 890 nm under a fluency of 50 mW/cm<sup>2</sup>. Experimental data were acquired using PHySpecV2 software (photon etc.) resulting in a three-dimensional data cube with both spatial and spectral features.

## 2.4 | Modeling approach to decorrelate physical aspects of degradation from J-V parameters

First, J-V curves measured before and after degradation were fitted [31] with a two-diode model [32]:

$$J(V) = J_{ph} - J_{01} \left( e^{\frac{q(V+JR_S)}{n_1 k_B T}} - 1 \right) - J_{02} \left( e^{\frac{q(V+JR_S)}{n_2 k_B T}} - 1 \right) - \frac{V + JR_S}{R_{sh}} \quad (1)$$

The fitting procedure employs least square reduction with the Levenberg–Marquardt algorithm and Jacobian scaling.

It allowed us to determine the series and shunt resistances ( $R_s$  and  $R_{sh}$ ), dark saturation current densities associated with  $n_1 = 1$  and  $n_2 = 2$  ( $J_{0,1}$  and  $J_{0,2}$ ), and photogenerated current density ( $J_{ph}$ ) for both measurements before (d0) and after (d9) aging. Ideality factor values were fixed to  $n_1 = 1$  and  $n_2 = 2$  to facilitate interpretation, so dark saturation current densities can be associated with radiative recombination and trap-assisted Shockley–Read–Hall (SRH) recombination, respectively. Moreover, these constraints on the fitting procedure limit the possibility of multiple valid parameter sets. Fits were performed with the same procedure and constraints for all samples, before and after aging. This consistency minimizes the impact of possible multiple optimal fits on the comparative study of fresh and aged samples done hereafter.

Second, calculations were carried out to distinguish the role of the diode parameters ( $J_{ph}$ ,  $J_{0,1}$ ,  $J_{0,2}$ ,  $R_s$ , and  $R_{sh}$ ) on the open circuit voltage  $V_{oc}$ , short-circuit current  $J_{sc}$ , and fill factor FF. For instance, the impact of  $R_s$  on  $V_{oc}$ ,  $J_{sc}$ , and FF was investigated by computing hypothetical  $V_{oc}^*(R_s)$ ,  $J_{sc}^*(R_s)$ , and  $FF^*(R_s)$  from the two-diode model, with degraded  $R_s$  (d9) while all other diode parameters retained their values as they were before aging (d0):

$$J^*(V) = J_{ph}^{d0} - J_{01}^{d0} \left( e^{\frac{q(V+J^*R_s^{d9})}{k_B T}} - 1 \right) - J_{02}^{d0} \left( e^{\frac{q(V+J^*R_s^{d9})}{2k_B T}} - 1 \right) - \frac{V + J^*R_s^{d9}}{R_{sh}^{d0}} \quad (2)$$

This expression was used to compute a hypothetical J-V curve, from which  $V_{oc}^*(R_s)$ ,  $J_{sc}^*(R_s)$ , and  $FF^*(R_s)$  were obtained. A similar approach was employed for each diode parameter. The impact of each parameter was then represented as a fraction of the total degradation. In the example on  $R_s$ , the ratios of the impact of  $R_s$  in the degradation of  $V_{oc}$ , FF, and  $J_{sc}$  are expressed as:

$$\frac{V_{oc}^*(R_s) - V_{oc}^{d0}}{V_{oc}^{d9} - V_{oc}^{d0}} \quad (3a)$$

$$\frac{FF^*(R_s) - FF^{d0}}{FF^{d9} - FF^{d0}} \quad (3b)$$

$$\frac{J_{sc}^*(R_s) - J_{sc}^{d0}}{J_{sc}^{d9} - J_{sc}^{d0}} \quad (3c)$$

## 3 | RESULTS

### 3.1 | Cells performance loss during aging with and without pollutant

#### 3.1.1 | Evolution of J-V curve parameters

The first step of our approach consisted of evaluating the effect of pollutants by comparing PV performances (J-V curves, EQE) of SLG/Mo/CIGS/Zn(O,S)/ZnMgO/AZO/NiAlNi cells, during temperature and humidity solicitations with and without (NH<sub>4</sub>)<sub>2</sub>SO<sub>4</sub>. The evolution of the power conversion efficiency (PCE), measured for 10 cells per module, is presented in Figure 2.

The average value and the standard deviation of the efficiency before and after 9 days of aging in three different conditions (ambient conditions “Reference”, T°C + RH “Blank”, T°C + RH + (NH<sub>4</sub>)<sub>2</sub>SO<sub>4</sub> “(NH<sub>4</sub>)<sub>2</sub>SO<sub>4</sub>”) are plotted in Figure 2A. It is clear from the comparison of the results of Reference d0 vs d9 samples, that the maximum efficiency loss for “Reference” modules does not exceed 10% of the initial performance after 9 days and remains within the error bars of the initial yield for 9 out of 10 cells (Figure 2A). The efficiency loss of the “Blank” module is much stronger: 37% of its initial performance (Figure 2A, compare Blank d0 vs d9). Rinsing the “Blank” cells modifies the performance very slightly, limiting the loss to 25% instead of 37% of the initial performance, mainly thanks to an improvement in the fill factor. In the presence of the ammonium sulfate (curves named “(NH<sub>4</sub>)<sub>2</sub>SO<sub>4</sub>”), only half of the cells could be measured with J-V because of the deterioration induced by the pollutant (bad contact, blocking of light, etc. ...). As the electrical measurements are certainly biased by the deposited pollutant, they are not included in Figure 2 but can be found in SI (Table S1). Curves named “d9 rinsed” show the results of the measurements repeated after the rinsing of the cells. Rinsing was necessary to wash out the soluble salt deposits and soluble corrosion products, allowing to decorrelate the impact of soluble corrosion products on the performance of the cell from the intrinsic degradation of the material and effects of insoluble products. It is clear from the figure, that although the “(NH<sub>4</sub>)<sub>2</sub>SO<sub>4</sub>” d9 rinsed module does not recover to the “Blank” level and keeps the efficiency loss of 58%, electrical measurements become possible for all the samples after rinsing. More than twice loss of the efficiency in the presence of

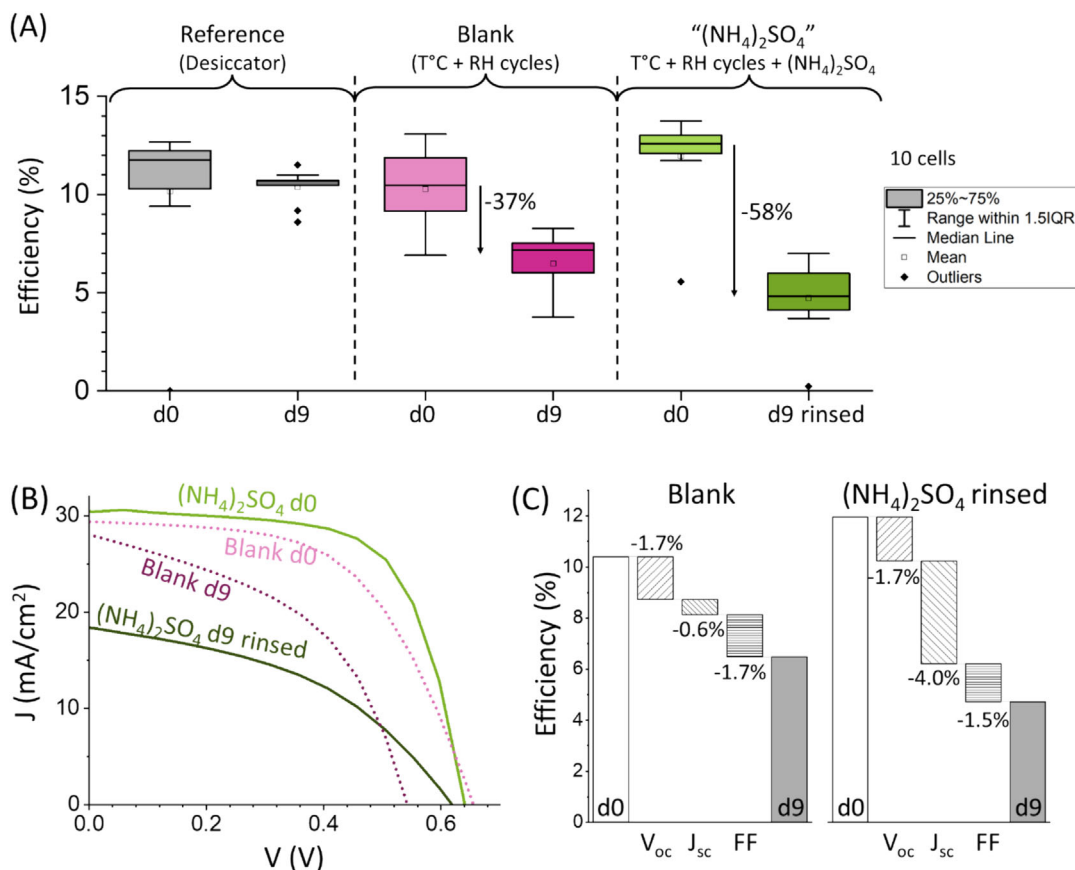


**FIGURE 2** (A) Power conversion efficiency of the cells before (“Reference”) and after aging with (“(NH<sub>4</sub>)<sub>2</sub>SO<sub>4</sub>”) and without (“Blank”) pollutant, (B) typical J-V curve of samples before (“d0”) and after (“d9”) aging and (C) average individual contributions of J<sub>sc</sub>, V<sub>oc</sub>, and FF on efficiency decline.

pollutants and significantly lower capacity to recover after rinsing highlight the detrimental effect of (NH<sub>4</sub>)<sub>2</sub>SO<sub>4</sub> on the reliability of CIGS solar cells.

The evolution of the electrical parameters in terms of J-V curves recorded before and after aging are plotted in Figure 2B. The waterfall chart presented in Figure 2C highlights the average individual contribution of each parameter (J<sub>sc</sub>, V<sub>oc</sub>, and FF) on the efficiency drop. Comparing Figure 2B and C, the efficiency loss of the “Blank” cells could be mainly attributed to the reduction of V<sub>oc</sub> and FF, as widely described in the literature for damp heat tests [33–35]. In the presence of (NH<sub>4</sub>)<sub>2</sub>SO<sub>4</sub>, a correct measurement was possible only after rinsing, so only the results obtained for rinsed cells are shown. One could note that the short circuit current is drastically reduced for the samples aged with the pollutant and can be considered to be responsible for more than half of the efficiency loss (see “(NH<sub>4</sub>)<sub>2</sub>SO<sub>4</sub> d9 rinsed” in Figure 2B). This indicates additional degradation mechanisms occurring due to the presence of (NH<sub>4</sub>)<sub>2</sub>SO<sub>4</sub>.

A detailed table containing the J-V parameters fitted with a two-diode model is included in SI, Table S1. The results of fitting will be analyzed in discussion, Section 4.

### 3.1.2 | Evolution of quantum efficiency (EQE, IQE)

EQE and IQE of the Blank and Reference cells are shown in Figure 3. They were quite similar when aged under similar conditions and only one representative curve of each sample is depicted. Both reflectance (Figure 3B) and normalized IQE (Figure 3A) look very little affected by aging for the Blank. A small systematic reduction of the “Blank” EQE (3% compared to “Reference”, obtained with correction after division by 1-Reflectance) could be explained by an increase in reflectance at the top of the cell or by an electrical degradation independent of the wavelength (see SI, Figure S2.A and B). This indicates that cyclic temperature and humidity aging without pollutants had little impact on the EQE.

The effect of (NH<sub>4</sub>)<sub>2</sub>SO<sub>4</sub> on the other hand is visible in multiple ways. First, if only one representative example is presented in Figure 3A, the EQE of the cells was largely different from one cell to another (variation can be seen in SI, Figure S2.C and S2.D). Second, the loss of interference fringes in the reflectance leads to a flattening of the spectrum (Figure 3B), also impacting the EQE (Figure S2.C and D), indicating a loss of the interference fringes in the presence of the pollutant. These effects are possibly due to the cell's surface

**FIGURE 3** (A) Normalized IQE and (B) 1-reflectance of the cells before (“reference”) and after aging for 9 days with (“(NH<sub>4</sub>)<sub>2</sub>SO<sub>4</sub>”) and without (“blank”) pollutant.

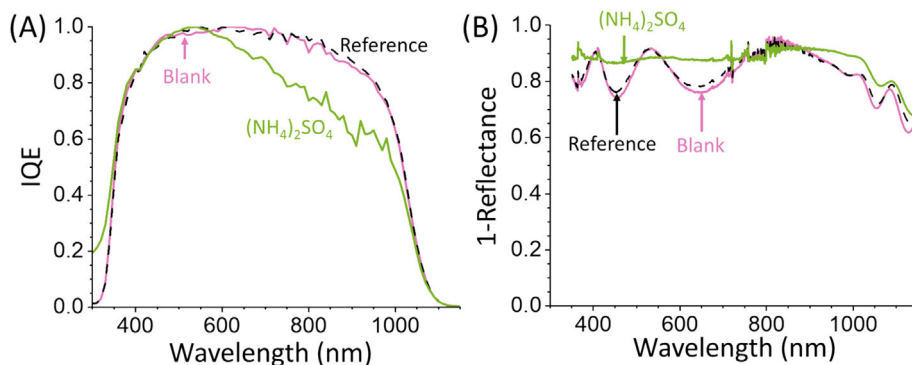
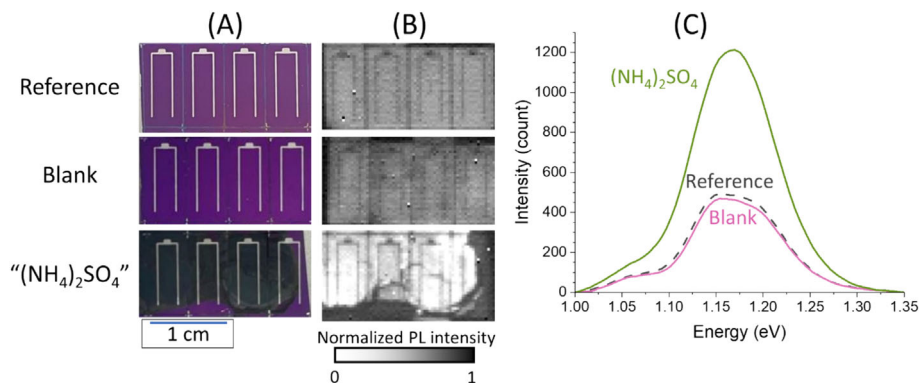


**FIGURE 4** (A) Visual images and (B) broadband integrated PL of cells before (“reference”) and after aging without and with the pollutant for 9 days (“blank” and “(NH<sub>4</sub>)<sub>2</sub>SO<sub>4</sub>” respectively) and (C) the corresponding averaged PL spectra.



roughness increase, which means that the transparent conductive oxide (TCO) made of AZO was affected. For some of the cells, this only impacted the EQE while their IQE was similar to the Reference (see Figure S2.C in SI). Optical losses in the reflectance spectra were also confirmed even after the removal of the pollutant by rinsing. The EQE transformation suggests that the TCO or at least its interface with the atmosphere was heavily affected by (NH<sub>4</sub>)<sub>2</sub>SO<sub>4</sub>. Lastly, in addition to the reflectance change, some cells presented a decrease of the IQE in the high wavelength region above 600 nm (Figure 3A). This indicates an incomplete collection of photogenerated carriers, possibly due to parasitic absorption probably due to corrosion products forming on the surface.

The  $J_{sc}$  values were calculated from the integration over all wavelengths of the EQE multiplied by the solar photon flux and are presented in Supporting Information, Table S1. The obtained values were in good agreement with the electrical measurements presented above. Compared to the Reference samples ( $J_{sc} = 28.4 \text{ mA/cm}^2$ ), only a small reduction was observed for the Blank ( $J_{sc} = 27.49 \text{ mA/cm}^2$ ) while a significant decrease occurred in the presence of (NH<sub>4</sub>)<sub>2</sub>SO<sub>4</sub> ( $J_{sc} = 22.5 \text{ mA/cm}^2$ ).

### 3.1.3 | Evolution of cell's photoluminescence (PL)

Hyperspectral PL spectra were recorded on the CIGS modules to evaluate the absorber optical quality of the sample aged for 9 days in a desiccator (“Reference”), in a climatic chamber with (“(NH<sub>4</sub>)<sub>2</sub>SO<sub>4</sub>”) and without pollutant (“Blank”). The results are shown in Figure 4.

Photographs and broadband-integrated PL images of the cells are presented in Figure 4A,B. The average PL signals of the three zones are presented in Figure 4C. The PL signals of the Reference and the Blank samples are quite homogenous over their surface (except the zones of the NiAlNi grid and scribing regions) and exhibit a large peak with a maximum at 1.15 eV and a shoulder at 1.06 eV. Indeed, the band gap of the CIGS varies from 1.11 eV to 1.22 eV due to a gallium gradient (GGI between 0.2 and 0.4, see calibrated GD-OES in Figure S3). The peak positions do not change during aging and only a slight reduction of about 10% is visible between the Reference and Blank signals intensities. This change is considered insignificant and can be attributed to the sample-to-sample variability. With (NH<sub>4</sub>)<sub>2</sub>SO<sub>4</sub>, the intensity of the PL is more than doubled compared to the Reference and Blank cases. This increase could be explained by two different hypothetical mechanisms: a passivation of the defects which improves the material quality or a texturing of the surface which increases the roughness and scatters more light. These hypotheses will be discussed later.

## 3.2 | Effect of aging on properties of individual layers: optical properties

In the presence of (NH<sub>4</sub>)<sub>2</sub>SO<sub>4</sub>, half of the cells' efficiency loss originated from the reduction of  $J_{sc}$  which may be attributed to an air/TCO interface modification and/or a change of the Mo's reflectivity. To evaluate these hypotheses, SLG/i:ZnO/AZO and SLG/Mo stacks were prepared, as shown in Figure 1B and aged for 14 days.

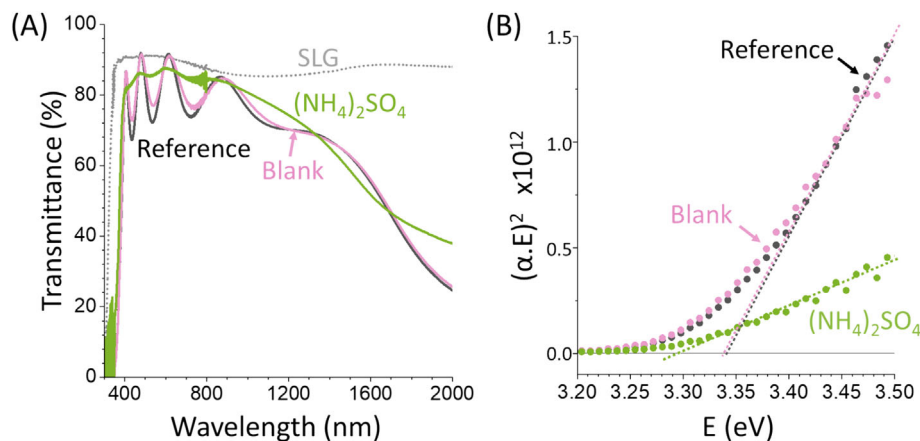


**FIGURE 5** (A) Transmittance spectra and (B) Tauc plot of rinsed SLG/i:ZnO/AZO after aging with (“(NH<sub>4</sub>)<sub>2</sub>SO<sub>4</sub>”) and without (“blank”) the pollutant for 14 days in comparison with undegraded “reference” samples.

### 3.2.1 | Evolution of the transparency of the TCO (AZO)

The transmittance of the SLG/i:ZnO/AZO samples is depicted in Figure 5A. For all samples, the presence of the interference fringes is due to the reflection occurring between SLG and ZnO. The amplitude of the “(NH<sub>4</sub>)<sub>2</sub>SO<sub>4</sub>” sample fringes is significantly reduced if compared to the “Reference”, in line with the evolution of the cell reflectance shown in Figure 3B. This suggests an increase in the film’s roughness. The transmittance remains high in the presence of (NH<sub>4</sub>)<sub>2</sub>SO<sub>4</sub> so the transparency modification of the TCO does not seem to be the critical change causing the  $J_{sc}$  reduction. Additionally, the “(NH<sub>4</sub>)<sub>2</sub>SO<sub>4</sub>” spectrum does not superimpose with the glass spectrum, which shows that the AZO layers were not completely dissolved. In conclusion, the pollutant increases the TCO’s roughness but does not decrease its transparency.

The refractive index of the AZO layer, calculated using the Swanepoel method [29], was 1.93 for the region from 400 to 600 nm, which is consistent with the literature [36]. The average thickness of the AZO layer was evaluated based on the spacing between the interference fringes as 600 nm for the “Reference”, 590 nm for the “Blank” and 670 nm for the “(NH<sub>4</sub>)<sub>2</sub>SO<sub>4</sub>” samples. A slight decrease in the “Blank” thickness compared to the “Reference” can be due to the dissolution of the layer while the increase with “(NH<sub>4</sub>)<sub>2</sub>SO<sub>4</sub>” against the “Reference” - to the deposition of corrosion products. These values should however be taken with caution, because of the inaccuracy of the data reading and the one-layer hypotheses used in calculation (in contrast to double ZnO/AZO structure).

The Tauc plots for the AZO samples are presented in Figure 5B, demonstrating a significant change in the linear part. Indeed, the calculated from the results optical band gap energy ( $E_g$ ) for both the “Reference” and the “Blank” is approximately 3.34 eV (or 371 nm) while for the “(NH<sub>4</sub>)<sub>2</sub>SO<sub>4</sub>”, the band gap is lower: near 3.29 eV (or 377 nm). It was hypothesized that this change is possibly an artifact caused by the Burstein–Moss Effect (increase in the TCO apparent optical band gap due to the band filling effect when doping the ZnO by Al [37,38]).

The carrier concentrations of the AZO samples were calculated from the plasma frequency  $\omega_p$ , see SI for more details about this calculation. The carrier concentrations were evaluated between 5 and  $7.7 \times 10^{20} \text{ cm}^{-3}$  for all three samples, which is consistent with the literature [37,39]. This method led to a very large range of values, insufficient to distinguish the samples but it is still consistent with the Hall effect results shown in Table 1.

In conclusion, analysis of the transmittance spectra of the AZO samples demonstrates that the pollutant increased the roughness of the TCO layer without degrading its optical properties (bandgap and carrier concentrations).

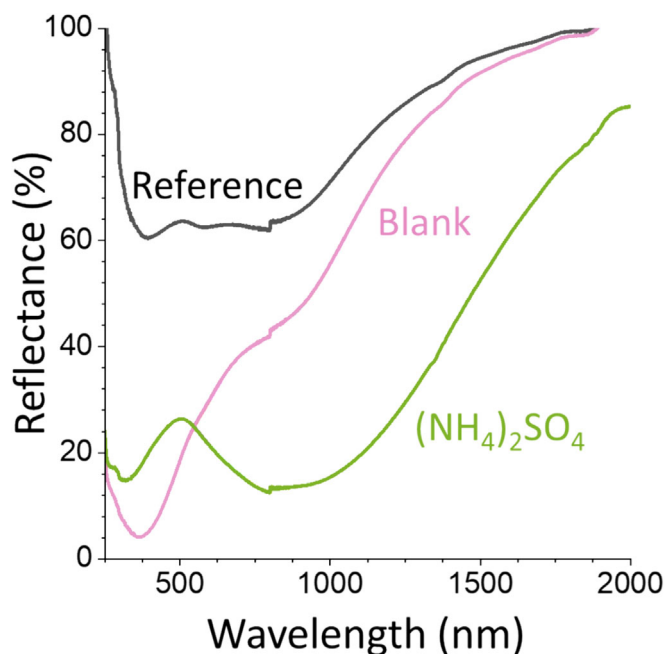
### 3.2.2 | Reflectivity of the back contact (Mo)

The Mo back contact reflectivity was evaluated by the reflectance measurement of SLG/Mo samples, presented in Figure 6. The Mo/CIGS reflectivity is critical in the case of a very thin absorber layer (<1  $\mu\text{m}$ ) where the back contact reflectance compensates for the low amount of photon absorbed in CIGS [40].

The reflectance curve of the “Reference” Mo is in line with the literature [41]. After aging without pollutant (“Blank” sample) a strong reduction of reflectance is observed, especially in the 400 nm region with almost 55% loss, which is also consistent with the literature [42–44]. It is probable that the corrosion of the back contact led to the formation of species absorbing in the 400 nm region. The reflectance reduction is even stronger with (NH<sub>4</sub>)<sub>2</sub>SO<sub>4</sub> and a second local minimum appears around 800 nm, reducing the reflectance by approximately 50%. It can be due to the formation of other corrosion products in the presence of the pollutant. As the Mo layer mostly influences the EQE spectrum around 900–1,000 nm [45], the pollutant should be particularly detrimental to the performance of the device. Indeed, from the normalized IQE depicted in Figure 3, the main reduction of the  $J_{sc}$  occurs from 600 to 1,000 nm. Therefore, the reflectivity loss of Mo is consistent with the reduction in the IQE. However, the reflectivity of Blank Mo is also reduced in this wavelength range, with no effect on the IQE spectrum, so the attribution of the IQE loss to the back contact remains uncertain.

**TABLE 1**  $R_{\text{sheet}}$  measured by four-point probe and  $R_{\text{sheet}}$ , carrier concentration and mobility measured by hall effect of SLG/i:ZnO/AZO before and after aging with (“(NH<sub>4</sub>)<sub>2</sub>SO<sub>4</sub>”) and without (“blank”) pollutant for 14 days.

	$R_{\text{sheet}}$ ( $\Omega\cdot\text{Sq}^{-1}$ )	$R_{\text{sheet}}$ ( $\Omega\cdot\text{Sq}^{-1}$ )	Carrier concentration ( $\text{cm}^{-3}$ )	Mobility ( $\text{cm}^2\text{V}^{-1}\text{s}^{-1}$ )	$R_{\text{sheet}}$ ( $\Omega\cdot\text{Sq}^{-1}$ )
Samples	AZO	AZO rinsed	AZO rinsed		
Techniques	4-P probe	4-P probe	Hall	Hall	Hall
Reference	50.1 ± 0.7	-	-4.1E+20	7.2	44.5
Blank	59.7 ± 0.7	58.7 ± 0.5	-3.3E+20	7.1	54.6
(NH <sub>4</sub> ) <sub>2</sub> SO <sub>4</sub>	72.9 ± 3.0	76.8 ± 9.8	-3.6E+20	5.8	62.4

**FIGURE 6** Reflectance spectra of aged and rinsed SLG/Mo stacks after aging for 14 days with (“(NH<sub>4</sub>)<sub>2</sub>SO<sub>4</sub>”) and without (“blank”) pollutants compared to undegraded “reference”.

Additionally, zero transmittance was measured for all samples and wavelengths (not shown here) revealing that the degradation was not severe enough to completely destroy the layer.

To conclude, the Mo/air interface is far more impacted by aging than the TCO's transmittance and could contribute to the overall reduction in  $J_{\text{sc}}$  in the 600–1,000 nm region. However, this behavior cannot be directly extrapolated on the whole cell where Mo could react with Se from CIGS to form MoSe<sub>2</sub> which can modify the stability of the underlying Mo [46].

### 3.3 | Effect of aging on properties of individual layers: conductivity

Contact conductivity was investigated on representative stacks because the cell series resistance increased six times after the aging in the presence of (NH<sub>4</sub>)<sub>2</sub>SO<sub>4</sub> ( $R_s = 1.3 \Omega$  for aging without and  $R_s = 7.6 \Omega$  with the pollutant, see Table S1 in SI). Three layers play a

key role in the conduction of charges to their extraction, namely the Mo back contact, the front TCO contact made of AZO, and the front metallic grid composed of Ni and Al.

#### 3.3.1 | AZO transparent conductive oxide

The surface conductivity loss of the AZO was estimated by measuring  $R_{\text{sheet}}$  of the SLG/i:ZnO/AZO samples, either with a linear four-point probe or by Hall effect (Table 1). Though there is a slight mismatch between the two methods, the same order of magnitude and similar trends are visible. The sheet resistivity of the AZO increases by 20% of its initial value after aging, as described elsewhere [33,39,47,48]. The increase is even higher (+50%) in the presence of the pollutant. Taking into account that rinsing would not occur in the encapsulated cells or devices, it is interesting to learn more about hypothetical corrosion products formed on the surface. The sample tested without pollutants partly recovers its initial conductivity after rinsing. For the sample aged in the presence of pollutant no recovery of conductivity after rinsing occurs. Considering, that conductivity loss can be due to the deposition of resistive corrosion products and the recovery is a result of the dissolution of their soluble part, the corrosion products formed in the conditions of aging of the “Blank” are expected to be more soluble than the products formed in the presence of (NH<sub>4</sub>)<sub>2</sub>SO<sub>4</sub>. It should be noted that the surface of the rinsed samples was very heterogeneous and very high values of  $R_{\text{sheet}}$  were recorded locally in some places. These values are not reported in Table 1 and only the lowest resistivity values representative of a major part of the rinsed surface (more than 75%) are considered.

Though non-drastring, the drop in AZO conductivity seems to originate from the decrease of electron carrier concentration and mobility for aging in the presence of (NH<sub>4</sub>)<sub>2</sub>SO<sub>4</sub>, as determined by Hall measurements. These slight variations must be handled with care because they were calculated considering a constant thickness.

To sum up, the degradation of AZO by humidity and temperature without pollutants led to an increase in its resistivity, however rinsing partially restores its conductivity. In the presence of pollutants, the resistance increase was larger and did not recover, which indicates either the formation of an insoluble insulating compound or some etching of the AZO layer.

**TABLE 2** Sheet resistivity  $R_{\text{sheet}}$  from four-point probe of SLG/Mo and SLG/i:ZnO/AZO/NiAlNi aged during 14 days with  $(\text{NH}_4)_2\text{SO}_4$  and without (blank) pollutant compared to undegraded reference before and after rinsing. For Mo, part of the measurements with exceptionally high values different from most of the surface was disregarded. The fraction of considered measurements is presented near the measured value in parenthesis. More details are available in SI, Figure S4.

Samples	$R_{\text{sheet}}$ ( $\Omega \cdot \text{Sq}^{-1}$ )	% of points measured in this $R_{\text{sheet}}$ range	$R_{\text{sheet}}$ ( $\Omega \cdot \text{Sq}^{-1}$ )	% of points measured in this $R_{\text{sheet}}$ range	$R_{\text{sheet}}$ ( $\Omega \cdot \text{Sq}^{-1}$ )	$R_{\text{sheet}}$ ( $\Omega \cdot \text{Sq}^{-1}$ )
	Mo		Rinsed Mo		NiAlNi	Rinsed NiAlNi
Reference	$0.18 \pm 0.01$	97%	-	-	$0.046 \pm 0.003$	-
Blank	$0.21 \pm 0.07$	77%	$0.20 \pm 0.01$	100%	$0.043 \pm 0.002$	$0.043 \pm 0.002$
$(\text{NH}_4)_2\text{SO}_4$	$0.20 \pm 0.01$	65%	$0.22 \pm 0.04$	95%	*	*

\*too resistive to be measured.

### 3.3.2 | Mo back contact

The sheet resistivity of the SLG/Mo samples is presented in Table 2. The “Reference”  $R_{\text{sheet}}$  measurement can be verified by calculating the resistivity for a thickness of 480 nm:  $2.4 \times 10^{-3} \Omega \cdot \text{cm}^{-1}$  which is consistent with the literature [37,49]. The resistivity slightly increases after aging (+10%), and a little bit more in the presence of  $(\text{NH}_4)_2\text{SO}_4$  (+20%). While most values are around  $0.2 \Omega \cdot \text{sq}^{-1}$ , some highly resistive points were recorded (see Table 2, column % of points measured in this range of  $R_{\text{sheet}}$ ), most likely due to an accumulation of the insulating pollutant salt and/or corrosion products. For the unrinsed samples, about 30% of the measured values were far above  $0.25 \Omega \cdot \text{sq}^{-1}$  (refer to statistical details in SI, Figure S4). This indicates that the corrosion was heterogeneous, affecting some regions more than others, and probably generating insulating corrosion products. This is in line with the literature [42–44,47,50]. It is interesting to note that similar to the AZO, the “Blank” Mo sample partly recovers its initial performance after rinsing, while the “ $(\text{NH}_4)_2\text{SO}_4$ ” Mo does not recover. Again, the corrosion products formed in the presence of the pollutant seem to be less soluble than without  $(\text{NH}_4)_2\text{SO}_4$ . Overall, the variation of Mo resistivity is heterogeneous, but it is still negligible compared to the resistivity increase of the AZO layer.

### 3.3.3 | NiAlNi front metallic contact

The sheet resistivity of the SLG/i:ZnO/AZO/NiAlNi samples is detailed in Table 2. As with Mo, the difference between the values measured before and after aging without pollutants is negligible. A slight increase in the conduction of the Blank sample may be due to a thinning of the Ni layer, revealing the buried Al with its higher conductivity, but the change may not be significant either. If the values are stable before and after rinsing, the measurement of the contact with four-point probe was very difficult before rinsing and was simplified by the rinsing of the surface. In the case of  $(\text{NH}_4)_2\text{SO}_4$ , the sample was too resistive to be measured, even after rinsing. The presence of

the drop strongly reduced conductivity of NiAlNi making it difficult to contact the metal grid.

## 4 | DISCUSSION: APPLICATION OF NUMERICAL MODEL TO FORMULATE HYPOTHESES OF DEGRADATION MECHANISMS IN CIGS CELLS WITH AND WITHOUT $(\text{NH}_4)_2\text{SO}_4$

If both series and shunt resistances  $R_s$  and  $R_{sh}$  degraded during aging (except for  $R_s$  in “Blank” conditions which were kept constant), their final impact on the FF is not straightforward to quantify. Therefore, the impact of J-V parameters ( $J_{ph}$ ,  $J_{0,1}$ ,  $J_{0,2}$ ,  $R_s$ , and  $R_{sh}$ ) on  $V_{oc}$ , FF, and  $J_{sc}$  was calculated and further analyzed. The fitting of J-V curves at different stages of degradation (d0 and d9) allowed to extraction associated diode parameters ( $J_{ph}$ ,  $J_{0,1}$ ,  $J_{0,2}$ ,  $R_s$ , and  $R_{sh}$ ).

Using the numerical method explained in Section 2.4, we could identify which parameter is responsible for the loss of performance. Hypothetical values of  $V_{oc}$ , FF\*, and  $J_{sc}$ \* were computed considering that the degraded value (d9) is obtained by the degradation of one single diode parameter, while other parameters were maintained at their initial values (d0). The results are presented in Figure 7, showing the ratio between computed and experimental degradation of  $V_{oc}$ , FF or  $J_{sc}$  calculated based on equations (3.a), (3.b), and (3.c). The boxplot represents the statistical variation over the 10 cells of the modules (or less as some outliers were removed). From the analysis of such a figure, a candidate with the highest probability of being at the origin of the degradation is the closest to the black dotted line at 1. On the contrary, the parameters whose median is the closest to the grey zero line have the least impact on the performances.

For the blank cells (Figure 7A–C), the degradation of two parameters is well correlated with the experimental results:  $J_{0,2}$  for  $V_{oc}$ , and  $R_{sh}$  for FF and  $J_{sc}$ . In fact, it is expected for the  $V_{oc}$  to be more sensitive to variations of the Shockley-Read-Hall (SRH) recombination densities (associated to the  $J_{0,2}$ ) than to any other parameter. Therefore, complementary PL measurements were carried out to verify the

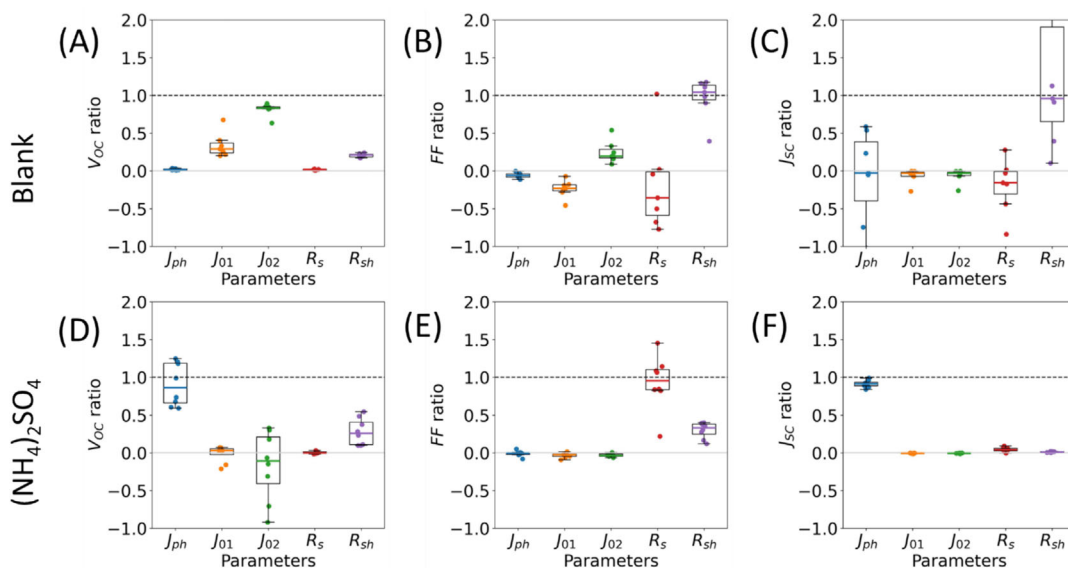


**FIGURE 7** Boxplots of ratios between computed and experimental values to assess the impact of each diode parameter ( $J_{ph}$ ,  $J_{0,1}$ ,  $J_{0,2}$ ,  $R_s$  and  $R_{sh}$ ) on the cell electrical performances for (A–C) “blank” and (D–F) “ $(NH_4)_2SO_4$ ” samples. The black dotted line symbolizes the case where computed degradation is compatible with 100% of experimental degradation.

hypothesis of the SRH recombination increase (see Figure 4). No significant change in the PL signal, either in the intensity or the peak position, was observed after aging. Therefore, the stable PL would not support a strong increase in the SRH recombination. As a result, the degradation of the  $R_{sh}$  appears to be the most plausible candidate to investigate further in this work, and the creation of shunt paths in the cell should be verified, especially near scribing or spots [6,34,51]. Further chemical investigation could give some hints about their presence and their role in the degradation.

For devices aged with pollutants (Figure 7D–F), two causes of degradation can be pointed out:  $J_{ph}$  for  $J_{sc}$  and  $V_{oc}$ , and  $R_s$  for FF. This is consistent with the results presented in Section 3.2, which showed that the  $J_{sc}$  was considerably influenced by the pollutant. Again, the FF is expected to be more sensitive to parasitic resistances ( $R_s$ ), and the  $J_{sc}$  to the photogenerated currents ( $J_{ph}$ ). The optical losses at the origin of the  $J_{sc}$  drop include soiling, change of reflectance of the cell or back contact, and transparency of the TCO [6,52]. The soiling effect of  $(NH_4)_2SO_4$ , due to the salt deposition on the surface of the cells, was evidenced during J–V measurement where half of the cells could not be measured correctly. Considering that  $(NH_4)_2SO_4$  is very soluble, the surface was rinsed to remove the salt and recover good contact thus isolating the effect of soiling and soluble species from other optical losses. Indeed, the  $J_{sc}$  of “ $(NH_4)_2SO_4$ ” cells after rinsing remained still lower than that of the Blank cells (as discussed in Section 3.1.1). If the optical loss is due to the TCO transparency loss because of the deposit of the pollutant, the transmittance curve is expected to decrease. Instead, when measured on the SLG/i:ZnO/AZO samples, a flattening of the interference fringes, linked to the increase in roughness, was observed (Figure 5). The destruction of the interference pattern is consistent with the reflectance measurement of the full cell shown in Figure 3B. Texturing of the TCO surface,

possibly by corrosion products, is also consistent with the increase in the PL signal observed in Figure 4. Indeed, the loss of the efficiency and the stable  $V_{oc}$  after aging with  $(NH_4)_2SO_4$  is in contradiction with an improvement of the material to explain this gain in the PL signal intensity so the increase in the roughness is the most probable hypothesis. A degradation of the Mo/air interface with aging was observed but the selenisation of Mo during CIGS deposition will impact the degradation process, and the layer will react less than the bare Mo [46]. The  $J_{sc}$  reduction can also be related to a bad collection of charges like contact corrosion on the electrodes.

As previously mentioned in Section 3.1, both the  $R_s$  and the  $R_{sh}$  were affected a lot by the aging with  $(NH_4)_2SO_4$ , making it uncertain about which of the two has the most impact on the FF. The calculations show here that the FF deterioration is mainly correlated to the  $R_s$  and only to a minor extent the  $R_{sh}$  (Figure 7D). This hypothesis can be verified by corroborating the results with the evolution of the electrical conductivity of the Mo, NiAlNi, and AZO contacts in the presence of  $(NH_4)_2SO_4$  analyzed in Section 3.3.

These results demonstrate that aging with temperature and humidity affects the conductivity of the Mo, AZO, and NiAlNi contacts, consistent with the literature for Mo [42–44,47,50] and AZO [8,33,48,53]. The samples with  $(NH_4)_2SO_4$  presented lower conductivity and higher variability of the  $R_{sheet}$ . This suggests a partial dissolution of the contacts or a heterogeneous formation of insulating non-soluble corrosion products, detrimental for the contact performance. Hall effect suggests a loss in carrier concentration to explain the loss of the  $R_s$  of the AZO. One can suggest that the change of the TCO band gap (Figure 5B) is an artifact caused by the Burstein–Moss Effect. Indeed, the Al doping of ZnO tends to increase its apparent optical band gap due to the band-filling effect [37,38]. However, even if a small change in the doping level was measured by

**TABLE 3** Main CIGS cell degradation mechanisms validated by corroboration of correlative models and physical characterizations of cells and representative layers.

Hypothesis	Samples	Sections	Impact on performance	
			“Blank”	“(NH <sub>4</sub> ) <sub>2</sub> SO <sub>4</sub> ”
(NH <sub>4</sub> ) <sub>2</sub> SO <sub>4</sub> specifically impacts the performance	Cells	[3.1.1] & [4]	$\eta = -37\%$	$\eta = -58\%$ after rinsing
$\downarrow J_{sc}$ due to optical loss	SLG/ZnO/AZO	[3.2.1]	$\rightarrow$ Transmittance	$\uparrow$ roughness
	SLG/Mo	[3.2.2]	$\downarrow$ Reflectivity	$\downarrow\downarrow$ Reflectivity
$\uparrow R_s$ due to contact corrosion	SLG/ZnO/AZO	[3.3.1]	+20% $R_{sheet}$	+50% $R_{sheet}$ and heterogenous
	SLG/ZnO/AZO/NiAlNi	[3.3.3]	$\rightarrow R_{sheet}$	$\uparrow\uparrow R_{sheet}$
$\downarrow V_{oc}$ not due to SRH recombination	Cells	[3.1.3]	$\rightarrow$ PL intensity	$\uparrow$ PL intensity ( $\uparrow$ roughness)

the Hall effect (Table 1), the difference is negligible between the “Blank” and the “(NH<sub>4</sub>)<sub>2</sub>SO<sub>4</sub>” samples and no difference in carrier concentration can be evidenced by plasma frequency. The doping level is thus insufficient to explain the reduction of the band gap. The loss of the contact conductivity, mainly in the AZO layer, seems to be the most reliable hypothesis to explain the increase in the cell's series resistance.

Thanks to the corroborative analysis of the results of correlative modeling and of the physical characterizations of the CIGS cells and representative stacks of the layers before and after degradation in different conditions, the degradation mechanisms, which could be considered the most important for the performance loss in different conditions could be proposed. The results of such an analysis are summarized in Table 3. Some questions are still not answered like the presence of shunt paths in the cell, the impact of sodium migration, and the exact nature of corrosion products at the origin of the degradation of performance.

## 5 | CONCLUSION

In the context of PV deployment in multiple environments like agrivoltaics or floating-PV, it is essential to consider the chemical environment, in particular atmospheric aerosol pollutants. Indeed, these environments can act on the PV materials and interfaces and, consequently on the overall performance of the device. If aerosols are usually disregarded in the PV industry tests, we proposed here a methodology considering the impact of the combined effect of temperature and humidity cycles and atmospheric aerosol pollutants on PV cells. The aging test consisted of the temperature and humidity cycles with and without a deposition of drops containing ammonium sulfate (NH<sub>4</sub>)<sub>2</sub>SO<sub>4</sub>, the pollutant largely known for the agricultural environment, on the top of samples.

Combining the evolution of the physical characteristics of the cells and representative stacks of layers during aging with the correlative modeling, the following conclusions could be drawn:

1. Strong detrimental effect of (NH<sub>4</sub>)<sub>2</sub>SO<sub>4</sub> on the CIGS cells reliability was evidenced. Indeed, in addition to the cell efficiency drop

observed after “usual” aging, i.e. temperature and humidity cycles (−37%), the presence of (NH<sub>4</sub>)<sub>2</sub>SO<sub>4</sub> degraded even more the performance (−58% after rinsing). This demonstrates that it is essential to take into account the atmospheric pollutants when considering the PV systems implantation in agricultural environments.

2. The computer model was used to formulate some hypotheses about the most important degradation mechanisms of the samples which appeared very different for the samples aged with and without the pollutant. With the temperature and humidity cycles only, the increase in recombination ( $J_{0,2}$  and  $J_{0,1}$ ) seems to be responsible for the reduction in  $V_{oc}$ , while the creation of shunt paths ( $R_{sh}$ ) could explain the loss in the FF and the  $J_{sc}$ . With the addition of the pollutant, optical losses ( $J_{ph}$ ) were proposed to explain the reductions of the  $J_{sc}$  and the  $V_{oc}$  while contact corrosion ( $R_s$ ) was suggested to impact the FF.
3. The hypotheses were verified by the experimental characterization of selected layers and interfaces. In terms of the evolution of the material properties, the PL analysis indicated that the loss of efficiency could be due to the formation of shunt pathways rather than an increase in defects quantity in the absorber. Optical losses ( $J_{sc}$ ) appear to be related to a loss of the interference fringes due to the surface roughness increase. The aged contacts showed a greater increase in the sheet resistance in the presence of pollutants than without it, which explains the increase in the  $R_s$ .

This thorough comprehensive study of the opto-electrical degradation of CIGS solar cells under agricultural-type environmental conditions opens questions on the chemical modifications, which could be at the origin of the electrical losses. This is under current investigation.

Finally, with the development of alternative PV usages (floating-PV, PV plants in industry sites...), this novel methodology must be applied to other environments (marine, industrial) by changing the nature of the model pollutants and PV technologies.

## DATA AVAILABILITY STATEMENT

The data that support the findings of this study are available from the corresponding author upon reasonable request.

## ORCID

Adèle Debono  <https://orcid.org/0009-0000-0515-0102>

Arthur Julien  <https://orcid.org/0000-0002-5395-0689>

Polina Volovitch  <https://orcid.org/0000-0001-5729-9830>

## REFERENCES

- Neher I, Buchmann T, Crewell S, Pospichal B, Meilinger S. Impact of atmospheric aerosols on solar power. *Metrolo Z.* 2019;28(4):305-321. doi:10.1127/metz/2019/0969
- Herman-Czezuch A, Mekeng AZ, Meilinger S, Barry J, Kimiaie N. Impact of aerosols on photovoltaic energy production using a spectrally resolved model chain: case study of southern West Africa. *Renew Energy.* 2022;194:321-333. doi:10.1016/j.renene.2022.04.166
- Saidan M, Albaali AG, Alasis E, Kaldellis JK. Experimental study on the effect of dust deposition on solar photovoltaic panels in desert environment. *Renew Energy.* 2016;92:499-505. doi:10.1016/j.renene.2016.02.031
- Radonjic I, Pavlovic T, Mirjanic D, Radovic M, Milosavljevic D, Pantic L. Investigation of the impact of atmospheric pollutants on solar module energy efficiency. *Thermal Sci.* 2017;21(5):2021-2030. doi:10.2298/TSCI160408176R
- Fountoukis C, Figgis B, Ackermann L, Ayoub MA. Effects of atmospheric dust deposition on solar PV energy production in a desert environment. *Solar Energy.* 2018;164:94-100. doi:10.1016/j.solener.2018.02.010
- Theelen M. *Degradation of cigs solar cells.* Technische Universiteit Delft; 2015.
- Debono A, L'Hostis H, Rebai A, et al. Synergistic effect between molybdenum back contact and CIGS absorber in the degradation of solar cells. *Progr Photovoltaics.* 2023;32(3):137-155. doi:10.1002/PIP.3742
- Zhang S et al. Importance of atmospheric aerosol pollutants on the degradation of Al<sub>2</sub>O<sub>3</sub> encapsulated Al-doped zinc oxide window layers in solar cells. *Progr Photovoltaics.* 2021;30(5):552-566. doi:10.1002/PIP.3527
- Spaes J. Photovoltaic shade for greenhouses. In: *PV Magazine* Accessed: Nov 22, 2023. [Online]. Available: <https://www.pv-magazine.com/2020/09/15/photovoltaic-shade-for-greenhouses/>
- Powelson DS, Dawson CJ. Use of ammonium sulphate as a sulphur fertilizer: implications for ammonia volatilization. *Soil Use Manage.* 2022; 38(1):622-634. doi:10.1111/sum.12733
- Ivanov A, Harizanova A. The use of ammonium sulphate has an adjuvant effect. *Sci Papers Series A Agronomy.* 2022;LXV(1):379-385.
- Committee on the Environment And Natural Resources, 'Atmospheric ammonia: sources and fate: a review of ongoing federal research and future needs'. 2000.
- Viatte C, Wang T, van Damme M, et al. Atmospheric ammonia variability and link with particulate matter formation: a case study over the Paris area. *Atmos Chem Phys.* 2020;20(1):577-596. doi:10.5194/acp-20-577-2020
- Ferm M, Granat L, Engardt M, et al. Wet deposition of ammonium, nitrate and non-sea-salt sulphate in Sweden 1955 through 2017. *Atmospheric Environment: X.* 2019;2:100015. doi:10.1016/j.aeoa.2019.100015
- Marchetto A, Simpson D, Aas W, et al. Good agreement between modeled and measured sulfur and nitrogen deposition in Europe, in spite of marked differences in some sites. *Front Environ Sci.* 2021;9: 734556. doi:10.3389/fenvs.2021.734556
- Murano K, Mukai H, Hatakeyama S, Oishi O, Utsunomiya A, Shimohara T. Wet deposition of ammonium and atmospheric distribution of ammonia and particulate ammonium in Japan. *Environ Pollut.* 1998;102(1):321-326. doi:10.1016/S0269-7491(98)80050-x
- Schuurkes JAAR. Atmospheric ammonium sulphate deposition and its role in the acidification and nitrogen enrichment of poorly buffered aquatic systems. *Experientia.* 1986;42(4):351-357. doi:10.1007/BF02118615
- Leygraf C, Graedel T. Atmospheric corrosion. In: *Electrochemical society series.* Second ed. Wiley; 2016. doi:10.1002/9781118762134
- Yilmaz P, de Wild J, Aninat R, et al. In-depth analysis of potential-induced degradation in a commercial CIGS PV module. *Progr Photovoltaics.* 2023;31(6):627-636. doi:10.1002/PIP.3670
- Gorji NE, Reggiani U, Sandrolini L. Peculiar role of holes and electrons in the degradation of CdTe thin films. *IEEE Trans Device Mater Reliab.* 2015;15(2):198-205. doi:10.1109/TDMR.2015.2414303
- Jahandardoost M, Walkons C, Bansal S. Degradation behavior of CIGS solar cells: a parametric analysis. *Solar Energy.* 2023;260:61-70. doi:10.1016/j.solener.2023.05.052
- Julien A, Puel J-B, Guillemoles J-F. Distinction of mechanisms causing experimental degradation of perovskite solar cells by simulating associated pathways. *Energ Environ Sci.* 2022;16(1):190-200. doi:10.1039/D2EE03377A
- Han C. Analysis of moisture-induced degradation of thin-film photovoltaic module. *Solar Energy Mater Solar Cells.* 2020;210:110488. doi:10.1016/j.solmat.2020.110488
- Kim Y, Shin M, Lee M, Kang Y. Hot-spot generation model using electrical and thermal equivalent circuits for a copper indium gallium selenide photovoltaic module. *Solar Energy.* 2021;216:377-385. doi:10.1016/j.solener.2021.01.042
- Rin N, Han C. Lifetime prediction method for moisture-induced degradation of glass-to-glass solar cell modules using spatially distributed diode model. *Solar Energy Mater Solar Cells.* 2021;225:111052. doi:10.1016/j.solmat.2021.111052
- Darvishzadeh P, Babanezhad M, Ahmadi R, Gorji NE. Modeling the degradation/recovery of open-circuit voltage in perovskite and thin film solar cells. *Mater Des.* 2017;114:339-344. doi:10.1016/j.matdes.2016.11.012
- Coyle DJ. Life prediction for CIGS solar modules part 1: modeling moisture ingress and degradation. *Progr Photovoltaics.* 2013;21(2): 156-172. doi:10.1002/PIP.1172
- Oth D, Ross R. Assessing photovoltaic module degradation and lifetime from long term environmental tests. In: *29th Institute of Environmental Science Annual Meeting;* 1983:121-126.
- Ahmed NM, Sauli Z, Hashim U, Al-Douri Y. Investigation of the absorption coefficient, refractive index, energy band gap, and film thickness for Al<sub>0.11</sub>Ga<sub>0.89</sub>N, Al<sub>0.03</sub>Ga<sub>0.97</sub>N, and GaN by optical transmission method. *Int J Nanoelectron Mater.* 2009;2:189-195.
- Ay L, Tolunay N. Optical transmission measurements on glow-discharge amorphous silicon nitride films. *Turk J Phys.* 2001;25(3):215-222.
- Suckow S. '2/3-Diode Fit'. Dec. 04, 2014. [Windows]. Available: <https://nanohub.org/resources/14300>
- Jagerl K, Isabella O, Smets A, van Swaaij R, Zeman M. *Solar energy - fundamentals, technology, and systems.* Delft University of Technology; 2014.
- de Amorim Soares G, Carolus J, Daenen M, et al. Round-robin of damp heat tests using CIGS solar cells. *Solar Energy.* 2021;214:393-399. doi:10.1016/j.solener.2020.11.048
- Nishinaga J, Kamikawa Y, Koida T, Shibata H, Niki S. Degradation mechanism of Cu(In,Ga)Se<sub>2</sub> solar cells induced by exposure to air. *Jpn J Appl Phys.* 2016;55(7):072301. doi:10.7567/JJAP.55.072301
- Schmidt M, Braunger D, Schaffler R, Schock HW, Rau U. Influence of damp heat on the electrical properties of Cu(In,Ga)Se<sub>2</sub> solar cells. *Thin Solid Films.* 2000;361-362:5-287. doi:10.1016/S0040-6090(99)00820-2
- Carron R, Avancini E, Feurer T, et al. Refractive indices of layers and optical simulations of Cu(In,Ga)Se<sub>2</sub> solar cells. *Sci Technol Adv Mater.* 2018;19(1):396-410. doi:10.1080/14686996.2018.1458579

37. Minami T. Transparent conductive oxides for transparent electrode applications. In: *Semiconductors and semimetals*. Vol.88. Elsevier; 2013:159-200. doi:[10.1016/B978-0-12-396489-2.00005-9](https://doi.org/10.1016/B978-0-12-396489-2.00005-9)
38. Shan FK, Yu YS. Band gap energy of pure and Al-doped ZnO thin films. *J Eur Ceram Soc*. 2004;24(6):1869-1872. doi:[10.1016/S0955-2219\(03\)00490-4](https://doi.org/10.1016/S0955-2219(03)00490-4)
39. Theelen M, Ntinas V, Steijvers H, Mannetje H, Vroon Z. The influence of glass substrates on the damp heat degradation of ZnO:Al films. *Thin Solid Films*. 2020;715:138429. doi:[10.1016/j.tsf.2020.138429](https://doi.org/10.1016/j.tsf.2020.138429)
40. Rezaei N, Isabella O, Vroon Z, Zeman M. Quenching Mo optical losses in CIGS solar cells by a point contacted dual-layer dielectric spacer: a 3-D optical study. *Opt Express*. 2018;26(2):A39. doi:[10.1364/OE.26.000A39](https://doi.org/10.1364/OE.26.000A39)
41. Jubault M, Ribeaucourt L, Chassaing E, Renou G, Lincot D, Donsanti F. Optimization of molybdenum thin films for electrodeposited CIGS solar cells. *Solar Energy Mater Solar Cells*. 2011;95:S26-S31. doi:[10.1016/j.solmat.2010.12.011](https://doi.org/10.1016/j.solmat.2010.12.011)
42. Pern J, Noufi R. An investigation of stability issues of ZnO and Mo on glass substrates for CIGS solar cells upon accelerated weathering and damp heat exposures. *DOE SETP Review Meeting*. 2007.p. 9.
43. Theelen M et al. Influence of deposition pressure and selenisation on damp heat degradation of the Cu (In,Ga)Se<sub>2</sub> back contact molybdenum. *Surf Coat Technol*. 2014;252:157-167. doi:[10.1016/j.surfcoat.2014.05.001](https://doi.org/10.1016/j.surfcoat.2014.05.001)
44. Karki S et al. Impact of water ingress on molybdenum thin films and its effect on Cu (In,Ga)Se<sub>2</sub> solar cells. *IEEE J Photovoltaics*. 2020;10(2): 696-702. doi:[10.1109/JPHOTOV.2019.2959947](https://doi.org/10.1109/JPHOTOV.2019.2959947)
45. Hegedus SS, Shafarman WN. Thin-film solar cells: device measurements and analysis. *Prog Photovolt: Res Appl*. 2004;12(23):155-176. doi:[10.1002/pip.518](https://doi.org/10.1002/pip.518)
46. Theelen M et al. The impact of selenisation on damp heat degradation of the CIGS back contact molybdenum. In: *In 2012 IEEE 38th Photovoltaic Specialists Conference (PVSC)*. IEEE; 2012:1-6. doi:[10.1109/PVSC-Vol2.2012.6656703](https://doi.org/10.1109/PVSC-Vol2.2012.6656703)
47. Lee D-W et al. Failure analysis of Cu (In,Ga)Se<sub>2</sub> photovoltaic modules: degradation mechanism of Cu (In,Ga)Se<sub>2</sub> solar cells under harsh environmental conditions: failure analysis of CIGS photovoltaic modules. *Prog Photovolt: Res Appl*. 2015;23(7):829-837. doi:[10.1002/pip.2497](https://doi.org/10.1002/pip.2497)
48. Theelen M et al. Physical and chemical degradation behavior of sputtered aluminum doped zinc oxide layers for Cu (In,Ga)Se<sub>2</sub> solar cells. *Thin Solid Films*. 2014;550:530-540. doi:[10.1016/j.tsf.2013.10.149](https://doi.org/10.1016/j.tsf.2013.10.149)
49. Theelen M, Daume F. Stability of Cu (In,Ga)Se<sub>2</sub> solar cells: a literature review. *Solar Energy*. 2016;133:586-627. doi:[10.1016/j.solener.2016.04.010](https://doi.org/10.1016/j.solener.2016.04.010)
50. Rajan G et al. Study of instabilities and degradation due to moisture ingress in the molybdenum back contact of Cu (In,Ga)Se<sub>2</sub> solar cells. In: *2018 IEEE 7th World Conference on Photovoltaic Energy Conversion (WCPEC) (A Joint Conference of 45th IEEE PVSC, 28th PVSEC & 34th EU PVSEC)*. IEEE; 2018:3037-3039. doi:[10.1109/PVSC.2018.8547368](https://doi.org/10.1109/PVSC.2018.8547368)
51. Villa S, Aninat R, Yilmaz P, et al. Insights into the moisture-induced degradation mechanisms on field-deployed CIGS modules. *Prog Photovolt Res Appl*. 2023;31(8):1-16. doi:[10.1002/pip.3689](https://doi.org/10.1002/pip.3689)
52. Tsanakas JA, Ha L, Buerhop C. Faults and infrared thermographic diagnosis in operating c-Si photovoltaic modules: a review of research and future challenges. *Renew Sustain Energy Rev*. 2016;62:695-709. doi:[10.1016/j.rser.2016.04.079](https://doi.org/10.1016/j.rser.2016.04.079)
53. Kempe MD, Terwilliger KM, Tarrant D. Stress induced degradation modes in CIGS mini-modules. In: *In 2008 33rd IEEE Photovoltaic Specialists Conference*. IEEE; 2008:1-6. doi:[10.1109/PVSC.2008.4922497](https://doi.org/10.1109/PVSC.2008.4922497)

## SUPPORTING INFORMATION

Additional supporting information can be found online in the Supporting Information section at the end of this article.

**How to cite this article:** Debono A, Fikree N, Julien A, et al. Impact of agricultural atmospheric pollutants on the optoelectrical performance of CIGS solar cells. *Prog Photovolt Res Appl*. 2024;32(11):814-826. doi:[10.1002/pip.3834](https://doi.org/10.1002/pip.3834)